Nuclear Science and Techniques (2025) 36:49
https://doi.org/10.1007/s41365-024-01623-x

Integral experiment on slab ^{nat}Pb using D-T and D-D neutron sources to validate evaluated nuclear data

Kuo-Zhi Xu[1,2] · Yang-Bo Nie[1,2] · Chang-Lin Lan[2] · Yan-Yan Ding[1] · Shi-Yu Zhang[2] · Qi Zhao[1] · Xin-Yi Pan[1] · Jie Ren[1] · Xi-Chao Ruan[1,2]

Received: 22 March 2024 / Revised: 9 August 2024 / Accepted: 1 September 2024 / Published online: 31 January 2025

Abstract

Lead (Pb) plays a significant role in the nuclear industry and is extensively used in radiation shielding, radiation protection, neutron moderation, radiation measurements, and various other critical functions. Consequently, the measurement and evaluation of Pb nuclear data are highly regarded in nuclear scientific research, emphasizing its crucial role in the field. Using the time-of-flight (ToF) method, the neutron leakage spectra from three ^{nat}Pb samples were measured at 60° and 120° based on the neutronics integral experimental facility at the China Institute of Atomic Energy (CIAE). The ^{nat}Pb sample sizes were 30 cm × 30 cm × 5 cm, 30 cm × 30 cm × 10 cm, and 30 cm × 30 cm × 15 cm. Neutron sources were generated by the Cockcroft-Walton accelerator, producing approximately 14.5 MeV and 3.5 MeV neutrons through the T(d,n)^{4}He and D(d,n)^{3}He reactions, respectively. Leakage neutron spectra were also calculated by employing the Monte Carlo code of MCNP-4C, and the nuclear data of Pb isotopes from four libraries: CENDL−3.2, JEFF−3.3, JENDL−5, and ENDF/B-VIII.0 were used individually. By comparing the simulation and experimental results, improvements and deficiencies in the evaluated nuclear data of the Pb isotopes were analyzed. Most of the calculated results were consistent with the experimental results; however, a few areas did not fit well. In the (n,el) energy range, the simulated results from CENDL−3.2 were significantly overestimated; in the (n,inl)D and the (n,inl)C energy regions, the results from CENDL−3.2 and ENDF/B-VIII.0 were significantly overestimated at 120°, and the results from JENDL−5 and JEFF−3.3 are underestimated at 60° in the (n,inl)D energy region. The calculated spectra were analyzed by comparing them with the experimental spectra in terms of the neutron spectrum shape and *C*/*E* values. The results indicate that the theoretical simulations, using different data libraries, overestimated or underestimated the measured values in certain energy ranges. Secondary neutron energies and angular distributions in the data files have been presented to explain these discrepancies.

Keywords Integral experiment · Neutron leakage spectra · ^{nat}Pb · D-T and D-D neutron sources · Evaluated nuclear data

1 Introduction

An evaluated nuclear database provides vital information for designing nuclear devices and has been extensively used in nuclear power applications. Furthermore, nuclear data connect fundamental nuclear physics research and the implementation of nuclear technology. The precision, veracity, and dependability of nuclear data have influenced advancements in the nuclear sector. High-precision differential cross-section measurements can provide direct experimental data to improve the accuracy of nuclear data [1–4], and a high-quality integral experiment is also an effective method for verifying and improving the accuracy of nuclear data[5–8]. Integral experiments involve measurements

This work was supported by the National Natural Science Foundation of China (Nos. 11775311 and U2067205), the Stable Support Basic Research Program Grant (BJ010261223282), and the Research and Development Project of China National Nuclear Corporation.

✉ Yang-Bo Nie
nieyb@163.com

Chang-Lin Lan
lanchl@lzu.edu.cn

[1] Key Laboratory of Nuclear Data, China Institute of Atomic Energy, Beijing 102413, China

[2] School of Nuclear Science and Technology, Lanzhou University, Lanzhou 730000, China

of integral parameters that can be modeled accurately by computation with few assumptions and approximations. This approach ascertains disparities and insufficiencies by comparing experimental results with theoretical calculations using nuclear data evaluated from diverse libraries.

T(d,n)^{4}He and D(d,n)^{3}He are fundamental reactions in nuclear fusion and play crucial roles in designing and implementing future fusion-related products. Conducting irradiation experiments on various materials using fusion reactions and testing their properties are essential for future fusion technologies. Consequently, conducting neutronics experiments employing D-T and D-D neutron source devices is necessary [9–12].

Lead (Pb) is widely used as a radiation-shielding material in nuclear device design owing to its high density and high atomic number [13]. Lead walls and doors can effectively block and absorb gamma particles in reactors and radiation therapy rooms. Furthermore, Pb has a low melting point, exceptional thermal conductivity, and significant heat capacity, which enable it to quickly absorb and transfer heat, making it useful for cooling certain types of nuclear devices, such as Pb-based fast reactors [14] and spallation targets in accelerator-driven subcritical systems (ADSs) [15, 16]. Therefore, the quality of the nuclear data evaluated for Pb isotopes is crucial for designing numerous nuclear devices.

International shielding integral experiments have been performed using lead samples to evaluate the nuclear data quality of Pb isotopes; for example, in the 1970 s, Hansen from the Lawrence Livermore National Laboratory (LLNL) conducted time-of-flight (ToF) measurements of neutron leakage spectra from a lead sphere with a radius of 8.192 cm [17]. In 1985, Simakov, from the Institute of Physics and Power Engineering (IPPE) in Obninsk, Russia, used ^{252}Cf spontaneous fission and D-T neutron sources to measure leakage neutrons from lead spheres with radii of 20.000, 40.000, and 60.000 cm [18, 19]. In 1990, Maekawa et al. from the Japan Atomic Energy Research Institute (JAERI) used the FNS facility to measure the neutron ToF spectra from Pb slabs with thicknesses of 20.000, 40.000, and 60.000 cm, at 0°, 12.2°, 24.9°, 41.8° and 66.8° [20]. These experiments provided crucial data for assessing and enhancing the evaluation of Pb isotopes.

Previous study investigations revealed certain limitations compared to the experiments in this thesis. Specifically, Refs. [17, 19, 20] mainly relied on D-T neutron sources without using D-D neutron sources, resulting in a lack of data on the interaction between low-energy neutrons and materials. Additionally, this experiment is more comprehensive than those of previous studies in terms of material selection, sample size, and measurement angles. For data analysis and simulation, this experiment utilizes the MCNP-4C program and multiple nuclear databases for a comprehensive evaluation, providing a more thorough comparison, whereas most earlier experiments did not adopt such a multi-database comparison approach. Some discrepancies exist in the data for Pb across various evaluated databases, particularly in the double-differential cross-section data for emitted neutrons at large

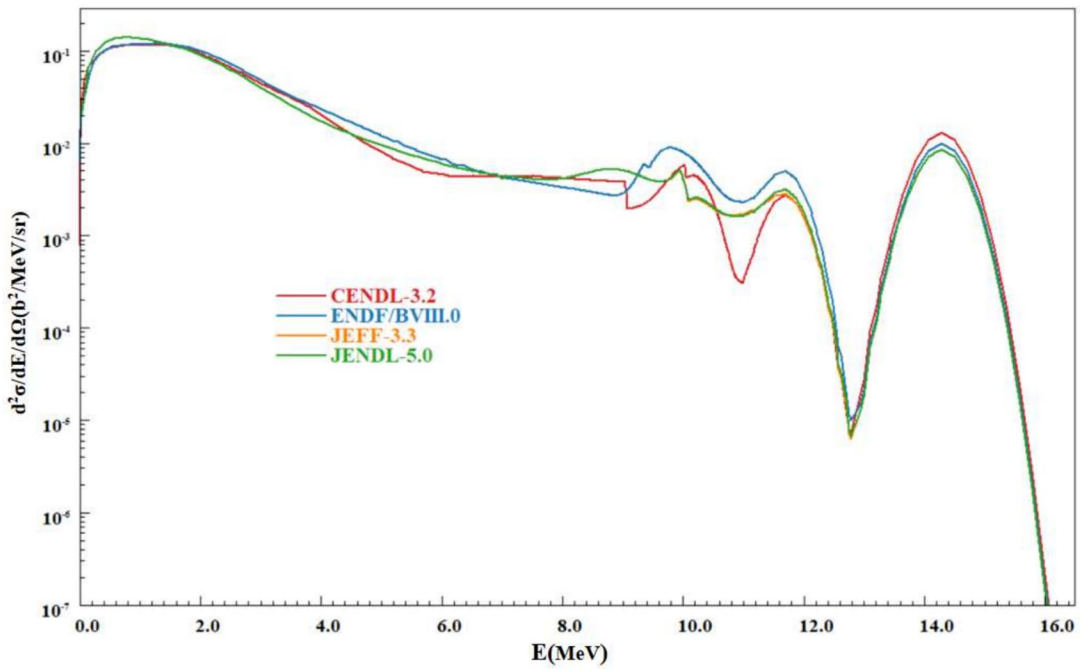

Fig. 1 (Color online) The emitted neutron energy spectra at 120° from different databases

angles, as shown in Fig. 1. This is primarily because no integral experimental results for the leakage neutron spectra at large angles are available internationally.

In this study, a new shielding integral experiment with slab ^{nat}Pb samples was conducted using pulsed D-T and D-D neutron sources. The neutron leakage spectra were measured at 60° and 120° using the ToF method. The simulation results of the leakage spectra were calculated by the MCNP-4C program [21] using the nuclear data of Pb isotopes from CENDL−3.2 [22], JEFF−3.3 [23], JENDL−5 [24], and ENDF/B-VIII.0 [25]. Problems with the nuclear data of Pb isotopes from CENDL−3.2 were analyzed by comparing the differences between the measurements and calculations.

This paper begins with an introduction outlining the research background and questions being investigated, followed by a detailed description of the experimental design and Monte Carlo (MC) simulation process in the Methods section, ensuring the reliability and validity of the study. The Data Processing section provides a comprehensive explanation of the data handling methods and uncertainty analysis. The Results section presents specific findings from the data analysis, including comparisons between the experimental data and data from various databases, leading to several conclusions. Finally, the Conclusion section summarizes the main discoveries and contributions of this study.

2 Methods

2.1 Experimental setup

Experiments were conducted at the CIAE by utilizing an integral experimental facility used previously for comparable experimental measurements [26–31]. Figure 2 illustrates the layout of the experimental setup. A 5.080 cm diameter stilbene scintillation crystal (SSC) was positioned on the dashed lines 2 and approximately 8.000 m away from the target, and a BaF_2 scintillation crystal was used to match the SSC, located approximately 4.000 m from the target, to monitor the neutron source pulse shape. Neutron leakage from the slab samples was detected using a BC501-A neutron detector with a diameter of 5.080 cm and a thickness of 2.540 cm, positioned behind a concrete wall at a flight path of 7.900 m perpendicular to the D^+ beam line and installed in a Pb house.

2.1.1 Neutron source

The experiments were conducted on the D-T and D-D neutron sources.

A T-Ti target was bombarded with a pulsed deuteron beam accelerated to 300 keV using the CIAE Cockcroft-Walton accelerator, with a beam current of ~ 20 μA. The beam pulse was repeated frequently at a rate of 1.5 MHz, and its pulse width was as narrow as 2 ns at the full width at half maximum (FWHM). The energy of the pulsed neutron beam was 14.5 MeV with a yield of 2×10^9 n/s. An associated

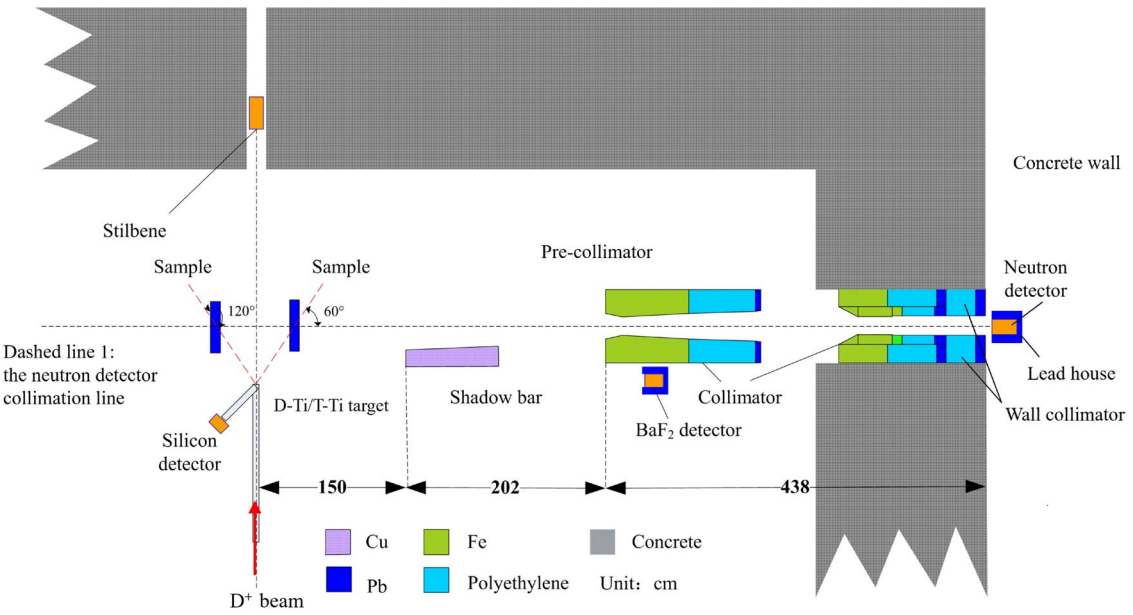

Fig. 2 (Color online) Layout diagram of integral experiment with ^{nat}Pb samples

particle system was installed at 12.2° using an Au-Si surface barrier semiconductor detector to monitor the neutron yield. Alpha particles were produced at opposite angles, although the T(d,n)^{4}He reaction produces neutrons. The semiconductor detector was used to measure alpha particles in the $\Delta\Omega$ solid angle at the ϕ angle to the incident deuteron beam, representing the neutron flux in the unit solid angle at the θ angle to the incident deuteron beam, which can be obtained by [32, 33]

$$\phi_{\mathrm{n}}\left(\theta, E_{\mathrm{d}}\right) = \frac{N_{\alpha}}{\Delta\Omega} \times A_{\alpha}, \tag{1}$$

$$\Delta\Omega = \frac{\pi \times r^2}{L^2}, \tag{2}$$

where N_{α} represents the count of alpha particles measured at ϕ angle, A_{α} represents the correction factor related to the energy of the deuteron beam and the emission angle of the alpha particles, and $\Delta\Omega$ represents the solid angle of the semiconductor detector subtending the T-Ti target, with r and L representing the radius of the aperture and the distance between the aperture and the target, respectively.

The relationship between $\phi_{\mathrm{n}}\left(\theta, E_{\mathrm{d}}\right)$, determined using Eq. (1), and the neutron yield from the T(d,n)^{4}He reaction is given by

$$\frac{\phi_{\mathrm{n}}(\theta)}{N_{\mathrm{n}}} = \frac{\sigma(\theta)}{\sigma_{\mathrm{tot}}}, \tag{3}$$

where N_{n}, σ_{tot}, and $\sigma(\theta)$ represent the source neutron yield and the total cross-section of T(d,n)^{4}He reaction and differential cross-section of T(d,n)^{4}He reacts at the θ angle, respectively. Substituting Eqs. (1) and (2) into Eq. (3), we can calculate the number of neutrons produced by the T(d,n)^{4}He reaction using

$$N_{\mathrm{n}} = \frac{N_{\alpha} \times A_{\alpha} \times \sigma_{\mathrm{tot}}}{\Delta\Omega \times \sigma(\theta)}, \tag{4}$$

The energy of the deuteron beam(E_{d}) for the D-T neutron source is ~ 300 keV, alpha particles are measured at 135°(ϕ =135°), neutrons are emitted at 0°(θ =0°), σ_{tot} is 3984 mb, $\sigma(\theta)$ is 336 mb/sr, and A_{α} is assumed to be 1.263. The radius of the aperture is ~ 0.160 cm, and the distance between the semiconductor detector and target was 90 cm. Based on this data, the relationship $N_{\mathrm{n}} = N_{\alpha} \times 1.508 \times 10^6$ can be obtained.

The D-D neutron source was obtained by replacing the T-Ti target with a D-Ti target. The deuteron beam current was~ 30 μA with an energy of ~ 360 keV. The energy of the pulsed neutron beam was ~ 3.2 MHz with a yield of 4.5×10^7 n/s. The neutron yield was measured using an associated particle system. For the D(d,n)^{3}He reaction, the associated protons were measured using competing D(d,p)T reactions [34]. This is because the protons produced in the D(d, p)T reaction are easier to detect compared with the ^{3}He from the D(d,n)^{3}He reaction. The accompanying ^{3}He particles have very low energy, approximately 0.9 MeV, making them easily drowned out by noise, whereas protons have relatively higher energy, approximately 3 MeV, which allows them to be completely separated from the noise. A semiconductor detector was used to measure protons in the $\Delta\Omega$ solid angle at ϕ angle to the incident deuteron beam, representing the neutron flux in the unit solid angle at the θ angle to the incident deuteron beam, which can be obtained by [35]

$$\phi_{\mathrm{n}}\left(\theta, E_{\mathrm{d}}\right) = \frac{N_{\mathrm{p}}}{\Delta\Omega} \times A_{\mathrm{p}}. \tag{5}$$

The neutron yield from the D(d,n)^{3}He reaction is obtained by substituting Eq. (5) and (2) into Eq. (3).

$$N_{\mathrm{n}} = \frac{N_{\mathrm{p}} \times A_{\mathrm{p}} \times \sigma_{\mathrm{tot}}}{\Delta\Omega \times \sigma(\theta)}, \tag{6}$$

where N_{p} represents the count of protons measured at ϕ angle and A_{p} represents the correction factor related to the energy of the deuteron beam, the emission angle of the protons, and the ratio of proton to neutron reaction cross-sections. σ_{tot} represents the total cross-section of the D(d,n)^{3}He reaction, and $\sigma(\theta)$ represents the differential cross-section of the D(d,n)^{3}He reaction at the θ angle.

For the D-D neutron source, the energy of the deuteron beam is ~ 360 keV, the associated particles are measured at 135°(ϕ=135°), with neutrons emitted at 0°(θ =0°), σ_{tot} is 40.300 mb, $\sigma(\theta)$ is 6.800 mb/sr, and A_{p} is assumed to be 2.557. Consequently, the relationship $N_{\mathrm{n}} = N_{\alpha} \times 1.526 \times 10^6$ can be obtained.

2.1.2 Sample

The slab samples used in the experiment included a polyethylene sample and three $^{\mathrm{nat}}$Pb samples. Polyethylene was used as a standard sample to test the reliability of the system, and its purity was ~> 99.9%. Information on the $^{\mathrm{nat}}$Pb samples is listed in Table 1, and its purity is greater than 99.99%.

2.1.3 Collimator

The neutrons interacted with the $^{\mathrm{nat}}$Pb sample and several other devices in the laboratory. The shields and collimators used in the experiment reduced the effects of scattered neutrons and environmental background on the experimental results [36]. Figure 2 shows a pre-collimator comprising iron, polyethylene, and Pb set between the sample and detector. A shadow bar made of copper was fixed between the

Table 1 Size, density, and composition of ^{nat}Pb samples

Sample	Size (cm)	Density (g/cm^3)	Nuclide (mass ratio, %)
^{nat}Pb	30 × 30 × 5	11.28	Pb(99.9971), Bi(0.0007), Fe+Ni+Cu+Zn+Ag+As+Sb+Sn +Cd(0.0022)
	30 × 30 × 10	11.31	
	30 × 30 × 15	11.30	

source neutrons and pre-collimator to eliminate the scattered neutron background generated by the interaction between the source neutrons and pre-collimator. Another collimator system was installed inside a concrete wall with a thickness of 2 m. Using a shadow bar, pre-collimator, and wall collimator, the background spectrum (sample-out) measured during the experiment was found to be significantly lower than the foreground spectrum (sample-in), as shown in Fig. 3. This effectively improved the foreground/background ratio by increasing it to approximately 20:1.

2.1.4 Detectors, electronic system, and data processing

An electronic circuit diagram is shown in Fig. 4. The leakage spectra were measured using a BC501-A detector. The output of the BC501-A detector was split into two channels: The first channel was sent to an analog-digital converter as pulse height (PH) information, whereas the second channel was used to determine details about the ToF and pulse shape discrimination (PSD). The start-time signal obtained from the anode signal of the detector was used to determine the ToF, whereas the stop signal was produced with an appropriate delay using the pulse pick-up signal from the accelerator. In the offline analysis, PH and PSD were used to determine the detection threshold and distinguish between the n and γ signals, respectively.

An SSC and BaF_2 scintillation crystal were used to detect the ToF spectra of the source neutrons and the associated gamma rays, respectively. By appropriately processing these spectra, the pulsed time distribution of the source neutrons was obtained. The SSD signal was the output of the semiconductor detector, which was used to obtain the count of associated particles as alpha particles or protons. All events from these detectors were recorded using the CAMAC data acquisition system. The Kmax software was used to obtain the initial leakage neutron ToF spectra after selecting an appropriate PH threshold and selecting neutron events by offline analysis. The initial spectra were normalized using neutron yields calculated from the count of the associated particles and the area of the BC501-A detector.

2.2 The simulations of Monte Carlo codes

MC simulations are an important part of integral experiments. Comparing the simulated and experimental results revealed discrepancies within the evaluated data, which validated the nuclear data. In this study, the MCNP-4C program was used to generate the ToF spectra of leakage neutrons. The neutron source and detector were accurately described to ensure precise simulation results.

2.2.1 Description of the neutron source

The neutron source characteristics include the energy spectra, angular flux, and pulsed time distributions. The T/Ti or D/Ti ratio, energy of the incident deuteron, energy distribution, and angular flux distribution were calculated based on the thickness of the T-Ti or D-Ti target using the

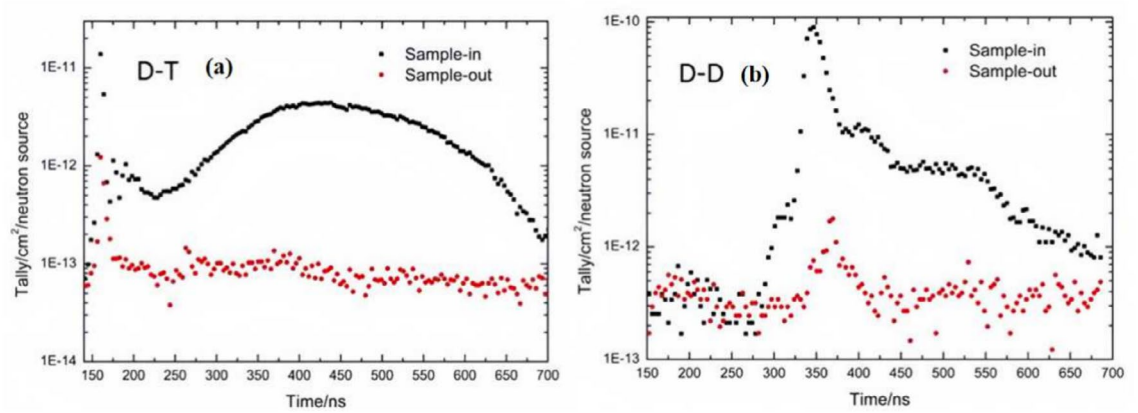

Fig. 3 **a** D-T and, **b** D-D ToF spectra measured under the sample in and sample out conditions

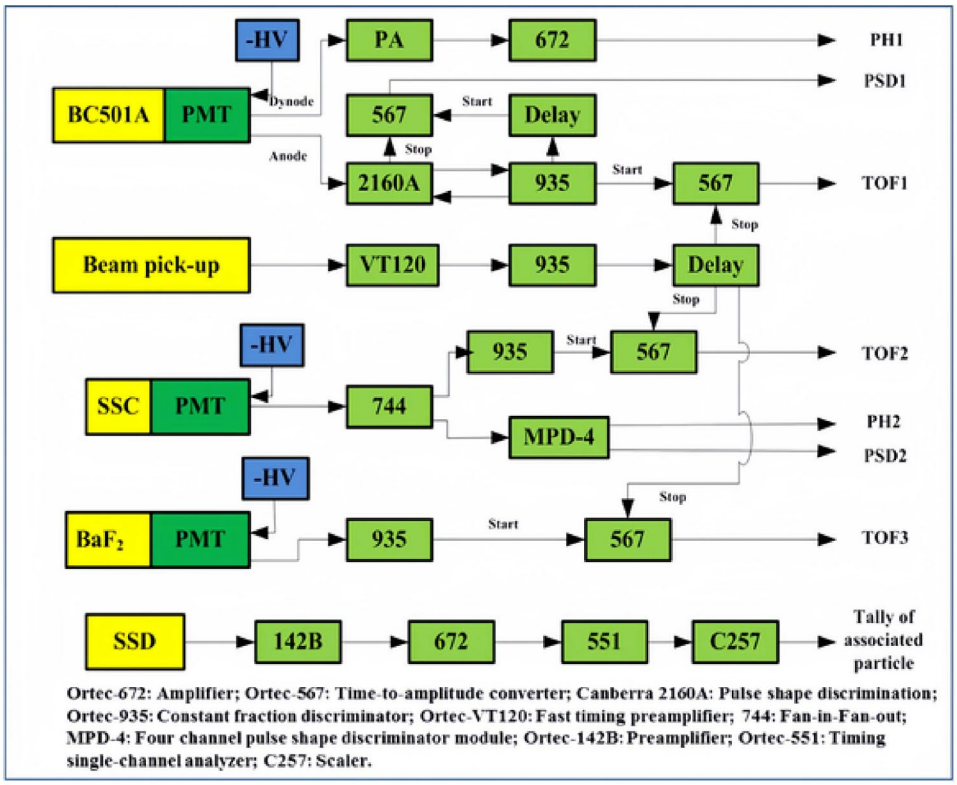

Fig. 4 Electronic circuit diagram for the experiment

TARGET [37] program developed by PTB in Germany. The thickness of the T-Ti and D-Ti targets used in the experiment was ~ 1 mg cm^{-2}, the T/Ti and D/Ti ratios were ~ 1.8, and the incident energy of the deuteron beam was 300 keV(D-T) or 360 keV (D-D). The results calculated using the TARGET program are shown in Fig. 5a and b.

The MCNP process requires an accurate pulse time distribution in the TME card. The accuracy of the pulse time distribution is extremely important for the final simulation of the ToF spectrum. Figure 5c shows the neutron ToF spectrum measured using stilbene and the gamma ToF spectrum measured using BaF_2. A new curve was fitted with an iterative algorithm using the SAND-II algorithm and the GRV-MC32 unfolding program [38]. In the processing procedure, the neutron ToF spectrum measured by the SSC detector served as the input spectrum, wherein the FWHM was larger than the actual pulse width owing to the structural characteristics of the neutron energy spectrum at 0°. The gamma ToF spectrum detected by the BaF_2 detector was used as the default spectrum in the iterative algorithm. The fitting results were compared with the input and default spectra in Fig. 5c, demonstrating that the bottom shape is similar to that of the input shape, whereas the peak shape of the fitting spectrum is similar to that of the default shape [39]. The final fitting spectrum provides a better description of the neutron pulse time distribution.

2.2.2 Description of the detector

This section describes the efficiency curve calibration and size specifications of the BC501-A liquid detector. The efficiency curve was determined experimentally using the following method [40]: (1) The relative efficiency curve was obtained using a ^{252}Cf neutron source. (2) The absolute efficiency value was calibrated using the D-D neutron source, and the result was used to normalize the relative curve. (3) The efficiency curve was calculated using an MC program with the NEFF code [41]. Figure 5d shows the efficiency curves for the different threshold values. The calculated results agree well with the experimental results. This study used a threshold value of 0.8 MeV. Detector size refers to the area and thickness of the detector. The detector can be defined as a surface detector in MCNP because its thickness is only 2.540 cm, which is significantly less than the flight distance of 8.000 m. Therefore, a ring detector estimator with a diameter of 5.080 cm was used to tally the ToF spectra in the MCNP-4C program.

2.3 Data processing

2.3.1 Simulated data

Two angles are calculated for the simulated model shown in Fig. 6a [42]. During the 60° and 120° simulations, the

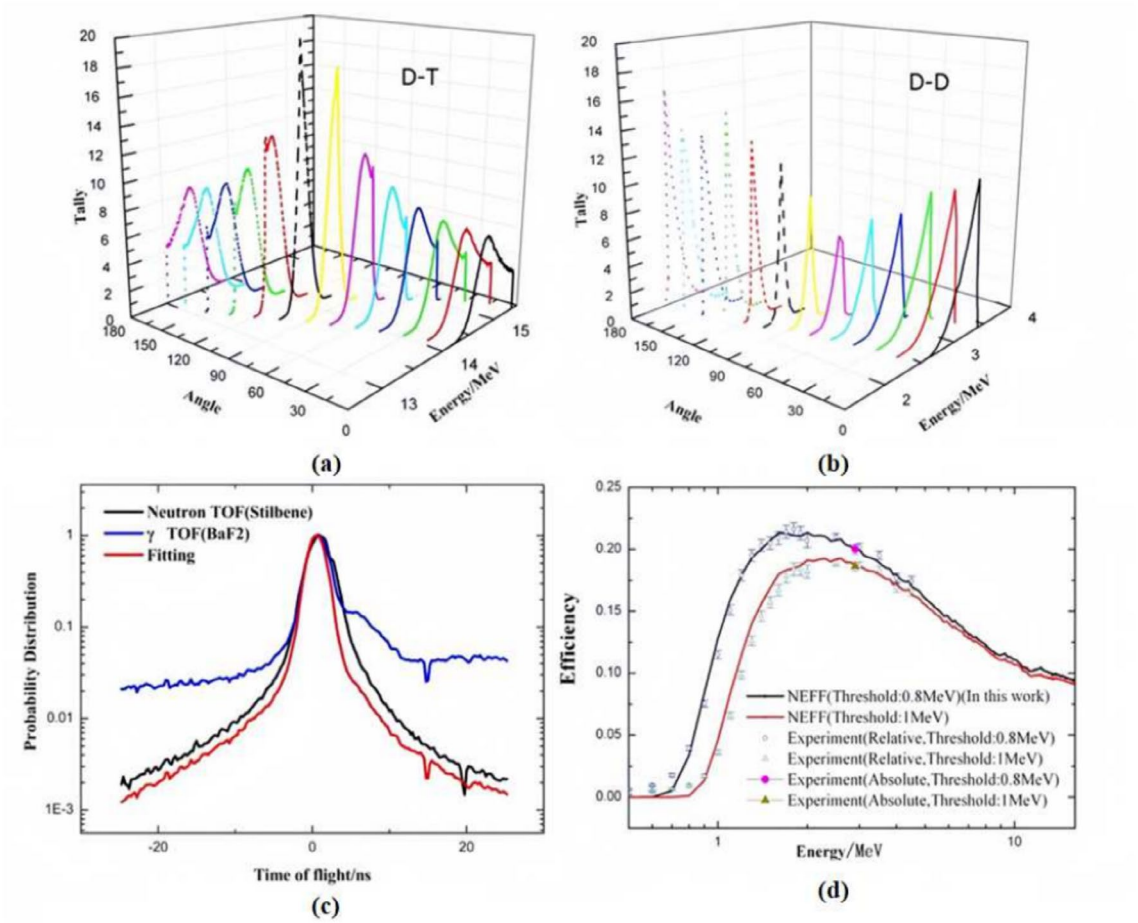

Fig. 5 (Color online) (**a**) The angle dependent energy distributions of D-T source (**b**) The angle dependent energy distributions of D-D source (**c**) The distributions of pulsed time (**d**) The neutron efficiency curves of BC501-A

left and right sample cells were filled with air, as with the background simulation. The evaluated nuclear data of the Pb isotopes from CENDL−3.2, JEFF−3.3, JENDL−5, and ENDF/B-VIII.0 were used to compare the simulated results from different libraries with the experimental results. The ACE libraries [43] were generated using the NJOY99 code [44]. The data for other materials, such as the target, collimators, shield, and air, were obtained from ENDF/B-VIII.0. Discrepancies can be easily identified by comparing the nuclear data evaluations described in the libraries above.

2.3.2 Measured data

The sample moved along the direction of the neutron detector collimation line (dashed line 1 in Fig. 2), transforming the measured angles owing to changes in the angle of the incident neutrons. In the data storage process, we adopted a method of cyclic measurements involving both samples and the background; for example, samples were measured for 2 h, followed by background measurements for another 2 h. This measurement prevented experimental deviations caused by beams or electronic fluctuations. The measured spectra need to be processed as follows before comparing the calculated spectra: (1) To verify the accumulated single experimental data, normalize each spectrum from the same sample and angle using the counts of the associated alpha or proton. (2) Compare each spectrum and discard the spectra that are noticeably different from those of the other rounds. (3) Utilize the remaining data to derive the summed foreground and background ToF spectra and normalize to one neutron using the neutron yield obtained from Eq. (4) or Eq. (6). (4) The background-corrected spectra can be obtained by subtracting the normalized background spectra from the normalized foreground spectra.

2.3.3 Test of the experimental system with standard samples

Leakage neutrons from two standard samples (polyethylene) were measured to verify the reliability of the measured data from the experimental system. A 30 cm × 30 cm × 6 cm polyethylene sample was selected

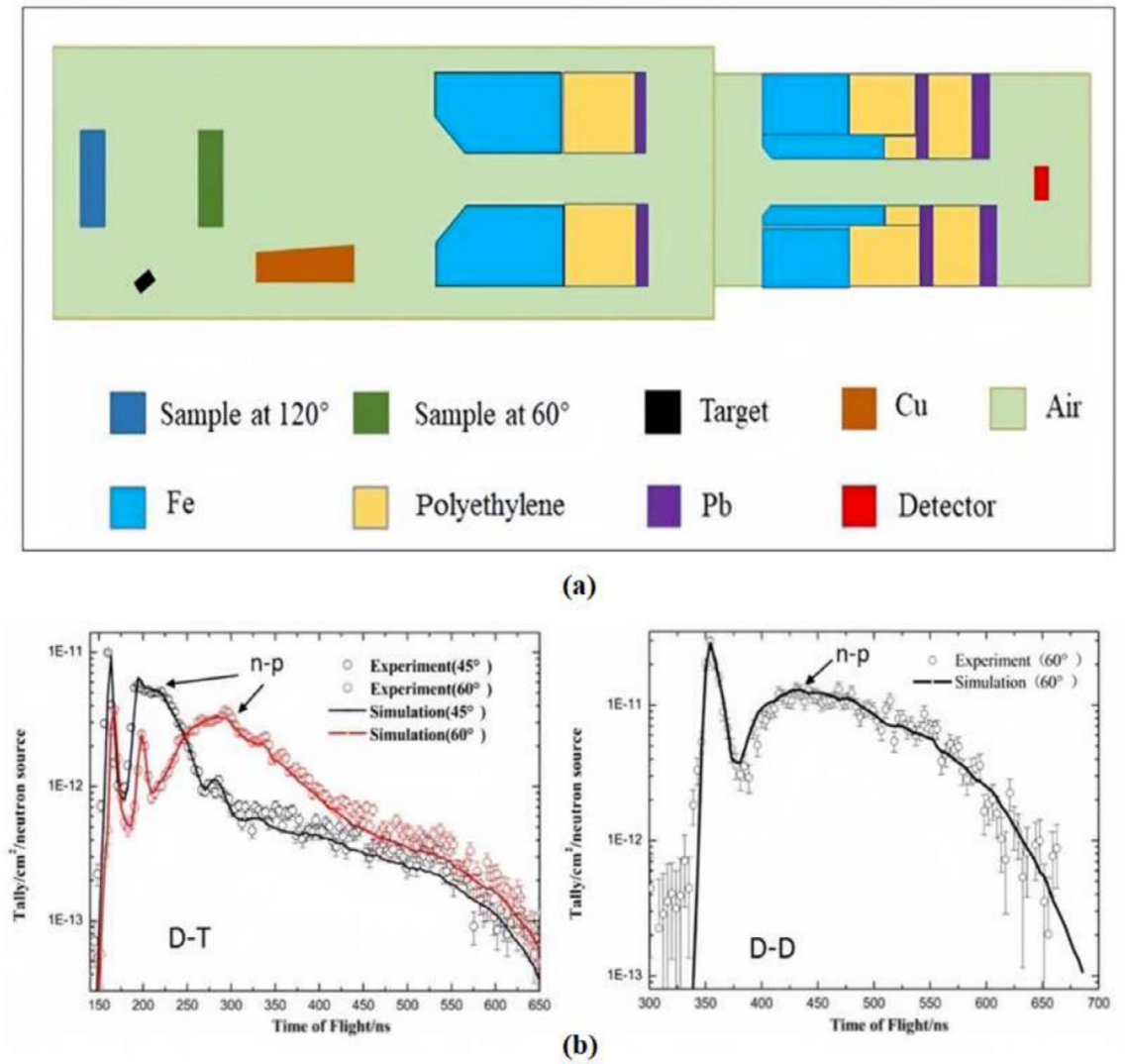

Fig. 6 (Color online) Simulation model and the ToF results from standard samples. **a** Simulation model for the MCNP calculations. **b** Comparison between experimental and simulated results of ToF spectra from the polyethylene sample

as the standard sample for the experiment with the D-T source, and the ToF spectra were measured in an orderly manner at 45° and 60°. Another polyethylene sample with dimensions of 30 cm × 30 cm × 2 cm was selected as the standard sample in the experiment with the D-D source, and the measurements were conducted at 60°[45].

The corresponding simulation results were obtained using the model shown in Fig. 6a; the evaluated data were all obtained from ENDF/B-VIII.0. The experimental and simulated results were compared after background rejection. The results are shown in Fig. 6b, and their counts in the n-p scattering peak are listed in Table 2. The experimental results of the n-p scattering peak agree well with the simulated results, indicating that the processing of the experimental data is reasonable and that the system measurement data are reliable.

Table 2 Results of the standard sample (per unit neutron and per detector area)

Neutron source	Angle	Measurement	Simulation	*C*/*E*
D-D	60°	$(4.56 \pm 0.28)\times10^{-10}$	4.59×10^{-10}	1.01 ± 0.046
D-T	45°	$(8.42 \pm 0.28)\times10^{-11}$	8.25×10^{-11}	0.981 ± 0.032
	60°	$(1.03 \pm 0.03)\times10^{-10}$	9.93×10^{-11}	0.960 ± 0.031

2.3.4 Uncertainty analysis of the experimental data

The initial experimental spectra can be normalized by the associated alpha or proton counts and by the ratio of the n-p

scattering peak area between the experimental and simulated results. The normalized coefficient B^1 can be obtained using

$$N_n = \frac{N_p^e}{N_p^c} = B^1 \times N_\alpha^p, \tag{7}$$

where N_p^e represents the sum of the neutron counts in the n-p scattering peak and N_p^c represents the area of the n-p scattering peak calculated by MCNP. Furthermore, N_α^p represents the count of associated particles detected in the standard sample. The initial experimental spectra from the ^{nat}Pb sample can be normalized using

$$\frac{N_{Pb}^e}{N_n} = \frac{N_{Pb}^e}{B^1 \times N_\alpha^{Pb}} = \frac{N_{Pb}^e \times N_p^c \times N_\alpha^p}{N_\alpha^{Pb} \times N_p^e}, \tag{8}$$

where N_{Pb}^e is the count of neutrons (per time bin) and N_α^{Pb} is the count of associated particles detected from the experiment with the ^{nat}Pb sample.

After normalizing the experimental data using Eq. (8), most systematic uncertainties, such as the uncertainty of the absolute detection efficiency (3%), were eliminated. Finally, the uncertainties in the experimental results comprised other systematic and statistical uncertainties. The systematic uncertainties include the relative detection efficiency ($\leq 3\%$) and scattering angle ambiguity ($\leq 1\%$), while the statistical uncertainties include the uncertainties of N_{Pb}^e, ($N_p^c \leq 0.5\%$), ($N_p^e \leq 0.5\%$), ($N_\alpha^p \leq 0.5\%$), and ($N_\alpha^{Pb} \leq 0.5\%$).

3 Results and discussion

3.1 Results based on the D-T source

The ToF spectra were measured at 60° and 120° using the D-T source and slab ^{nat}Pb samples. The experimental results were compared with those calculated from different evaluated data libraries, as shown in Fig. 7. According to the

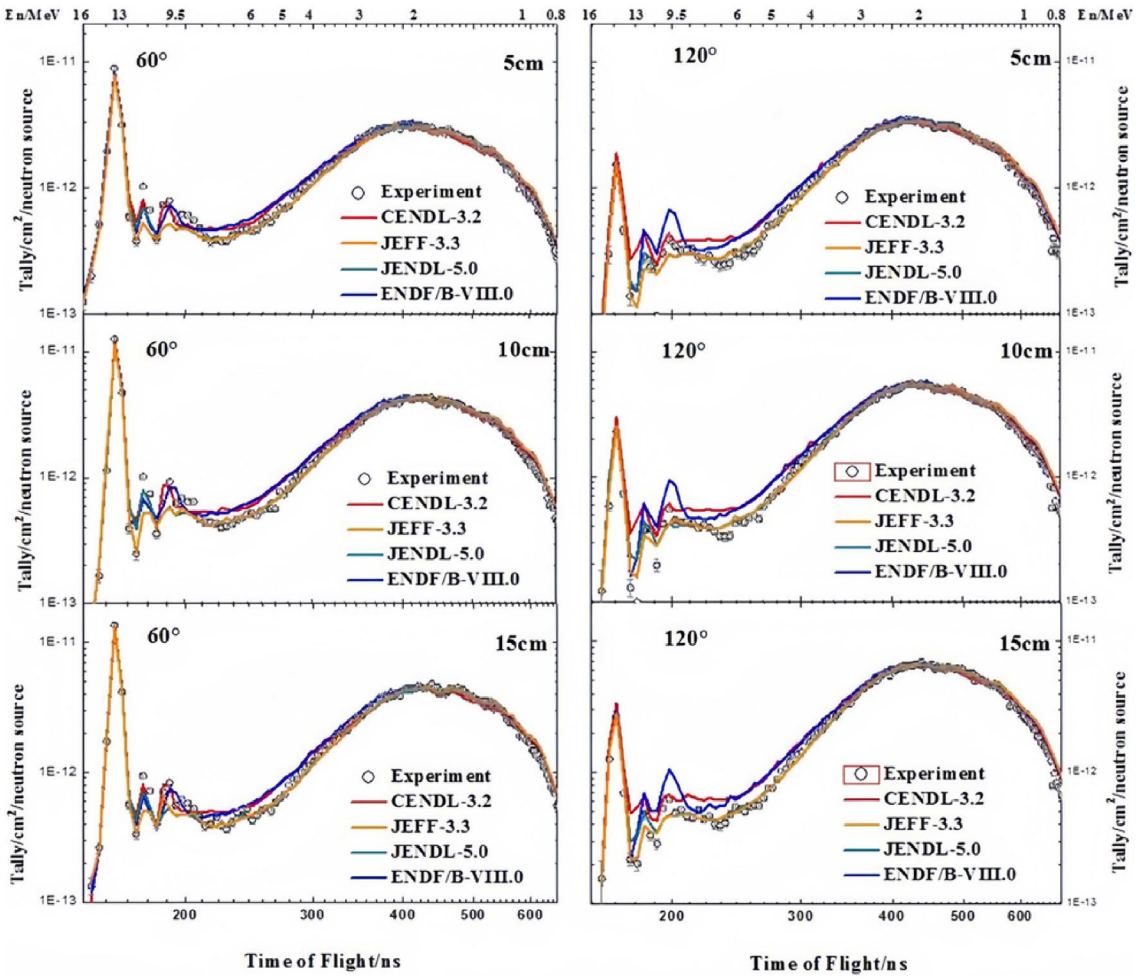

Fig. 7 The ToF spectra from the ^{nat}Pb sample after interaction with D-T neutrons

comparison, the simulations from CENDL−3.2 and ENDF/B-VIII.0 were obviously higher than the measurements at ~ 240 ns.

A study on the cross-section differences related to the production of secondary neutrons was conducted to determine the reason for the discrepancies between the experimental and calculated results. The ND-plot program is a simple and efficient application of the nuclear data processing software[46]. Experimental or evaluated data can be obtained by inputting the proton number, mass number, incident particle type, energy, and other information about the target nucleus, such as the reaction cross-section, secondary particle angle distribution, secondary particle energy distribution, and secondary particle energy angle distribution. Using this program, the secondary neutrons produced by the interaction of 14.5 MeV neutrons with the ^{nat}Pb sample are shown in Fig. 8a. These results indicate that the secondary neutrons comprise elastic scattering neutrons (n,el), inelastic scattering neutrons (n,inl), and (n,2n) reactions.

The neutron energy spectra can be divided into four energy regions based on the regions obtained from different reactions: (1) from 13 MeV to 16 MeV, the neutrons contributed from (n,el); (2) from 9.5 MeV to 13 MeV, the neutrons contributed from discrete level inelastic scattering ((n, inl)d); (3) from 6 MeV to 9.5 MeV, the neutrons contributed from continuous energy level inelastic scattering ((n,inl)C); (4) from 0.8 MeV to 6 MeV, the neutrons contributed from the (n,2n) reaction and multiple neutron scattering. Based on these energy regions, the simulation and measurement of the leakage neutron spectra were integrated, and the *C*/*E* values were derived by comparing the simulated and experimental results. The *C*/*E* ratios are listed in Tables 3 and 4.

In the (n,el) energy range, the simulated results from CENDL−3.2 were significantly overestimated in the 120° direction by 40%. Comparing the elastic scattering angle distribution data for the ^{nat}Pb samples from different libraries revealed that CENDL−3.2 yielded higher elastic scattering cross-section values at 120° than those from other libraries, as shown in Fig. 9a.

In the (n,inl)D energy region, the simulation results from CENDL−3.2 and ENDF/B-VIII.0 agree well with the measurements at 60°; however, they are significantly overestimated at 120°, particularly ENDF/B-VIII.0, which is overestimated by ~ 70%. The results from JENDL−5 and JEFF−3.3 showed better agreement at 120°; however, they were underestimated at 60°. Comparing the angular distribution

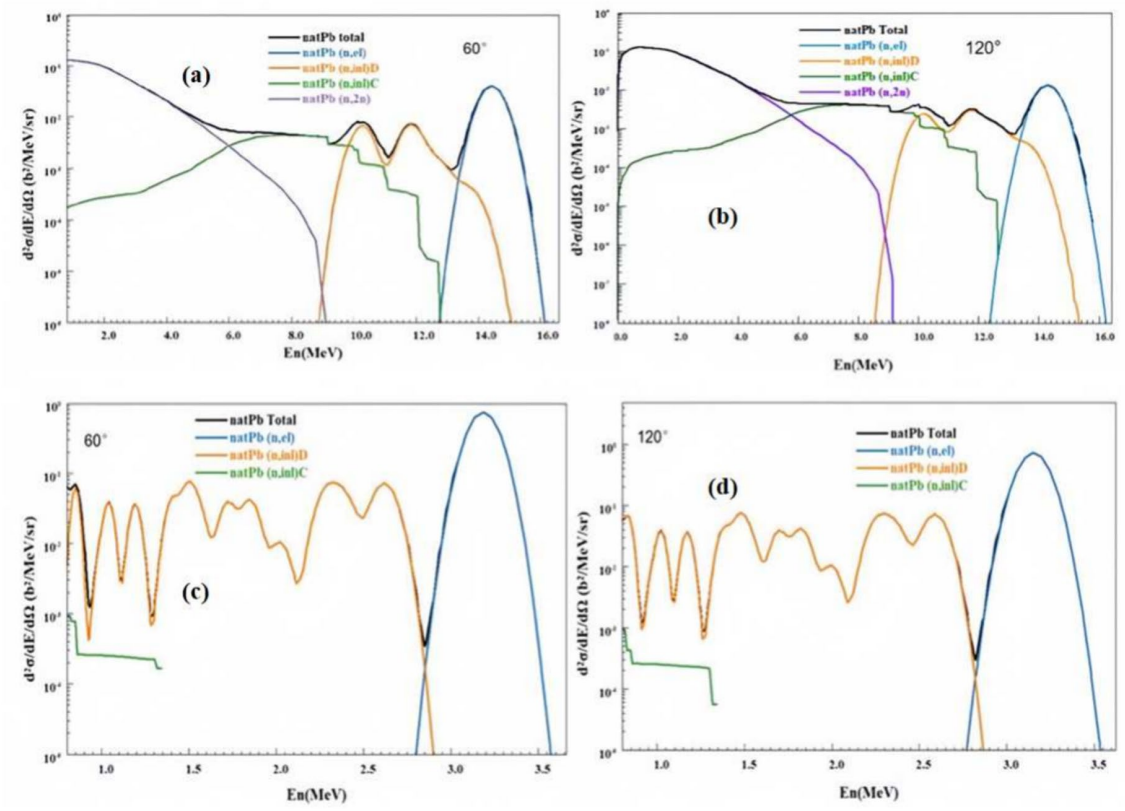

Fig. 8 (Color online) **a** Energy spectra of secondary neutrons at 60° after interaction of 14.5 MeV neutrons. **b** Energy spectra of secondary neutrons at 120° after interaction of 14.5 MeV neutrons. **c** Energy spectra of secondary neutrons at 60° after interaction of 3.2 MeV neutrons. **d** Energy spectra of secondary neutrons at 120° after interaction of 3.2 MeV neutrons(Data retrieved from CENDL−3.2 library)

Table 3 C/E values of four energy regions and the total energy region at 60°

Thickness (cm)	Energy (MeV)	Time (ns)	CENDL−3.2	JEFF−3.3	JENDL−5	ENDF/B-VIII.0
5 cm	13–16	151–167	0.948 ± 0.031	0.927 ± 0.031	0.926 ± 0.031	1.017 ± 0.034
	9.5–13	167–194	0.931 ± 0.034	0.703 ± 0.026	0.787 ± 0.029	0.886 ± 0.032
	6–9.5	194–242	1.054 ± 0.037	0.912 ± 0.032	0.917 ± 0.032	1.075 ± 0.038
	0.8–6	242–651	0.980 ± 0.031	1.001 ± 0.032	0.990 ± 0.031	1.040 ± 0.033
	0.8–16	151–651	0.979 ± 0.031	0.987 ± 0.031	0.979 ± 0.031	1.036 ± 0.033
10 cm	13–16	151–167	1.025 ± 0.033	0.977 ± 0.032	0.974 ± 0.032	1.010 ± 0.033
	9.5–13	167–194	0.994 ± 0.036	0.715 ± 0.026	0.831 ± 0.030	0.947 ± 0.034
	6–9.5	194–242	1.113 ± 0.039	0.949 ± 0.033	0.934 ± 0.033	1.102 ± 0.038
	0.8–6	242–651	1.006 ± 0.032	1.029 ± 0.032	1.016 ± 0.032	1.061 ± 0.033
	0.8–16	151–651	1.009 ± 0.032	1.019 ± 0.032	1.008 ± 0.032	1.057 ± 0.033
15 cm	13–16	151–167	1.019 ± 0.033	0.974 ± 0.032	0.979 ± 0.032	0.960 ± 0.031
	9.5–13	167–194	0.950 ± 0.035	0.741 ± 0.027	0.780 ± 0.029	0.859 ± 0.031
	6–9.5	194–242	1.079 ± 0.038	0.917 ± 0.032	0.913 ± 0.032	1.056 ± 0.037
	0.8–6	242–651	0.975 ± 0.031	1.005 ± 0.032	0.990 ± 0.031	1.033 ± 0.033
	0.8–16	151–651	0.979 ± 0.031	0.998 ± 0.031	0.985 ± 0.031	1.026 ± 0.032

Table 4 C/E values of four energy regions and the total energy region at 120°

Thickness (cm)	Energy (MeV)	Time (ns)	CENDL−3.2	JEFF−3.3	JENDL−5	ENDF/B-VIII.0
5 cm	13–16	157–174	1.428 ± 0.074	1.137 ± 0.059	1.093 ± 0.057	1.162 ± 0.060
	9.5–13	174–202	1.429 ± 0.070	0.912 ± 0.045	1.017 ± 0.050	1.758 ± 0.086
	6–9.5	202–252	1.372 ± 0.054	1.040 ± 0.041	1.042 ± 0.041	1.270 ± 0.050
	0.8–6	252–680	1.000 ± 0.032	1.018 ± 0.032	1.010 ± 0.032	1.063 ± 0.034
	0.8–16	157–680	1.014 ± 0.032	1.019 ± 0.032	1.011 ± 0.032	1.073 ± 0.034
10 cm	13–16	157–174	1.421 ± 0.059	1.147 ± 0.048	1.201 ± 0.050	1.159 ± 0.048
	9.5–13	174–202	1.414 ± 0.058	0.942 ± 0.039	1.013 ± 0.042	1.686 ± 0.070
	6–9.5	202–252	1.397 ± 0.050	1.059 ± 0.038	1.050 ± 0.038	1.280 ± 0.046
	0.8–6	252–680	1.022 ± 0.032	1.047 ± 0.033	1.034 ± 0.033	1.079 ± 0.034
	0.8–16	157–680	1.035 ± 0.033	1.047 ± 0.033	1.036 ± 0.033	1.087 ± 0.034
15 cm	13–16	157–174	1.352 ± 0.052	1.090 ± 0.042	1.115 ± 0.043	1.131 ± 0.044
	9.5–13	174–202	1.365 ± 0.054	0.911 ± 0.036	1.007 ± 0.040	1.635 ± 0.065
	6–9.5	202–252	1.360 ± 0.048	1.004 ± 0.035	1.016 ± 0.036	1.250 ± 0.044
	0.8–6	252–680	1.009 ± 0.032	1.037 ± 0.033	1.025 ± 0.032	1.064 ± 0.033
	0.8–16	157–680	1.020 ± 0.032	1.037 ± 0.033	1.026 ± 0.032	1.071 ± 0.034

of discrete-level inelastic scattering from different libraries (Fig. 9b) shows that ENDF/B-VIII.0 had the highest differential cross-section values around 120°, and JEFF−3.3 had the lowest values at ~ 60°.

In the (n,inl)C energy region, the simulation results from JENDL−5 and JEFF−3.3 agreed well with the measured results; however, the results from CENDL−3.2 and ENDF/B-VIII.0 were significantly overestimated at 120°. This is because the neutron spectra of (n,inl)C retrieved from CENDL−3.2 and ENDF/B-VIII.0 were higher than those of the other two from 6 MeV to 9 MeV, as presented in Fig. 9c.

In the 0.8 MeV to 6 MeV energy region, the simulations all agreed well with the measurements, and the total neutron fluxes between 0.8 MeV to 16 MeV and the C/E values were all very close to 1.000.

3.2 Results based on the D-D source

Leakage neutron spectrum measurements from the slab ^{nat}Pb samples based on the D-D source were obtained under similar experimental conditions. The experimental results were compared with those calculated from different evaluated data libraries, as shown in Fig. 10.

Using the NDPlot tool, secondary neutrons produced by the interaction of the D-D neutrons (~ 3.2 MeV) with the^{nat}Pb sample are shown in Fig. 8b. Combined with the

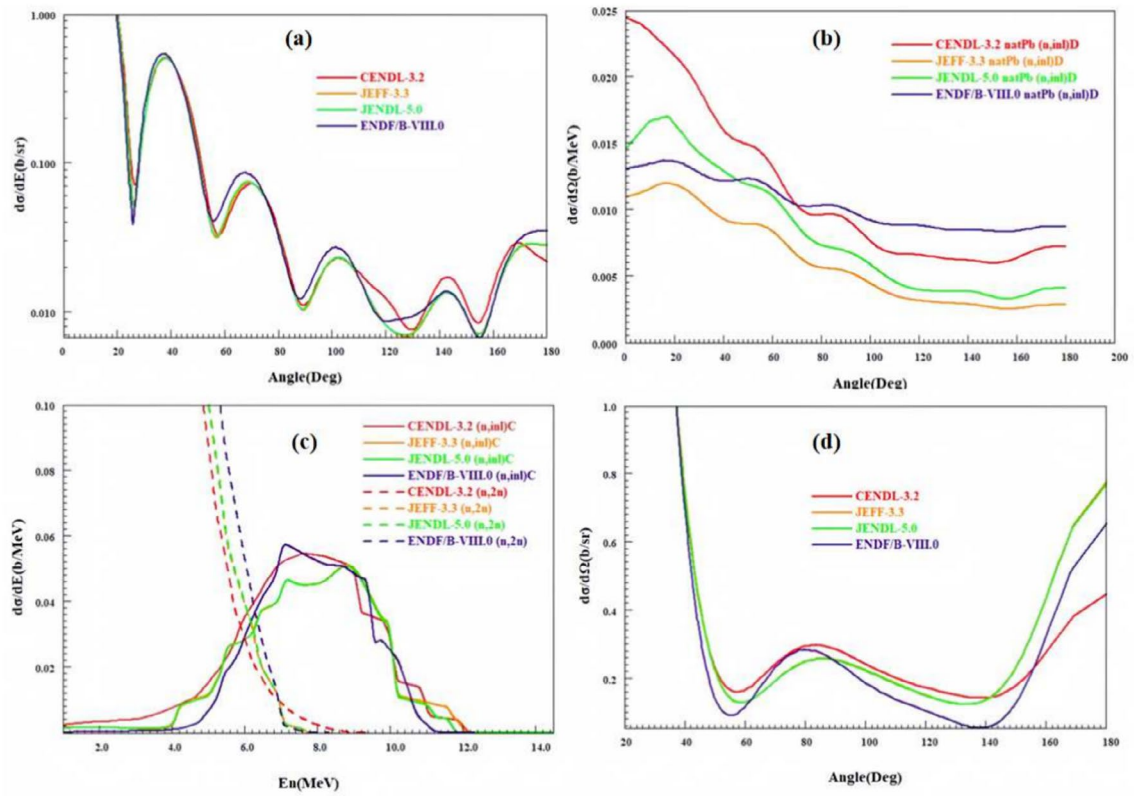

Fig. 9 (Color online) Data retrieved from different evaluation files after the interaction of 14.5 MeV and 3.2 MeV neutrons with the ^{nat}Pb samples

figure, the secondary neutrons are divided into two energy regions: (1) in the 2.8 MeV to 3.5 MeV region, the neutrons produced by the (n,el) reaction; (2) in the 0.8 MeV to 2.8 MeV region, the neutrons produced by the (n,inl)D reaction. The simulated and experimental results of the leakage neutron spectra were integrated according to the two energy regions above, and the corresponding C/E values are summarized in Table 5.

Figure 10 and Table 5 show that most of the calculated results from CENDL−3.2, JEFF−3.3, and JENDL−5 agree well with the experimental results, except for those from ENDF/B-VIII.0, which underestimated the experimental results by ~ 20% at 120° in the 2.8 MeV to 3.5 MeV region. The angular distributions of neutron elastic scattering for ^{nat}Pb after the interaction with 3.2 MeV neutrons are shown in Fig. 9d; the cross-section from ENDF/B-VIII.0 is lower than those from the remaining three libraries at 120°.

4 Conclusion

Integral experimental data from the ^{nat}Pb samples were obtained using the D-T and D-D neutron sources. The leakage neutrons from the ^{nat}Pb sample slabs were measured using the ToF method at angles of 60° and 120°. The leakage spectra were simulated by the MCNP-4C code using the nuclear data evaluated from CENDL−3.2, JEFF−3.3, JENDL−5, and ENDF/B-VIII.0. The measured and theoretical spectra were compared by focusing on their spectral shapes and *C*/*E* values in various energy regions. The comparison revealed that the calculated results from JENDL−5 exhibited a closer correspondence with the measured ones; in the (n,el) energy range, the simulated results from CENDL−3.2 were significantly overestimated; in the (n,inl)D and the (n,inl)C energy regions, the results from CENDL−3.2 and ENDF/B-VIII.0 were significantly

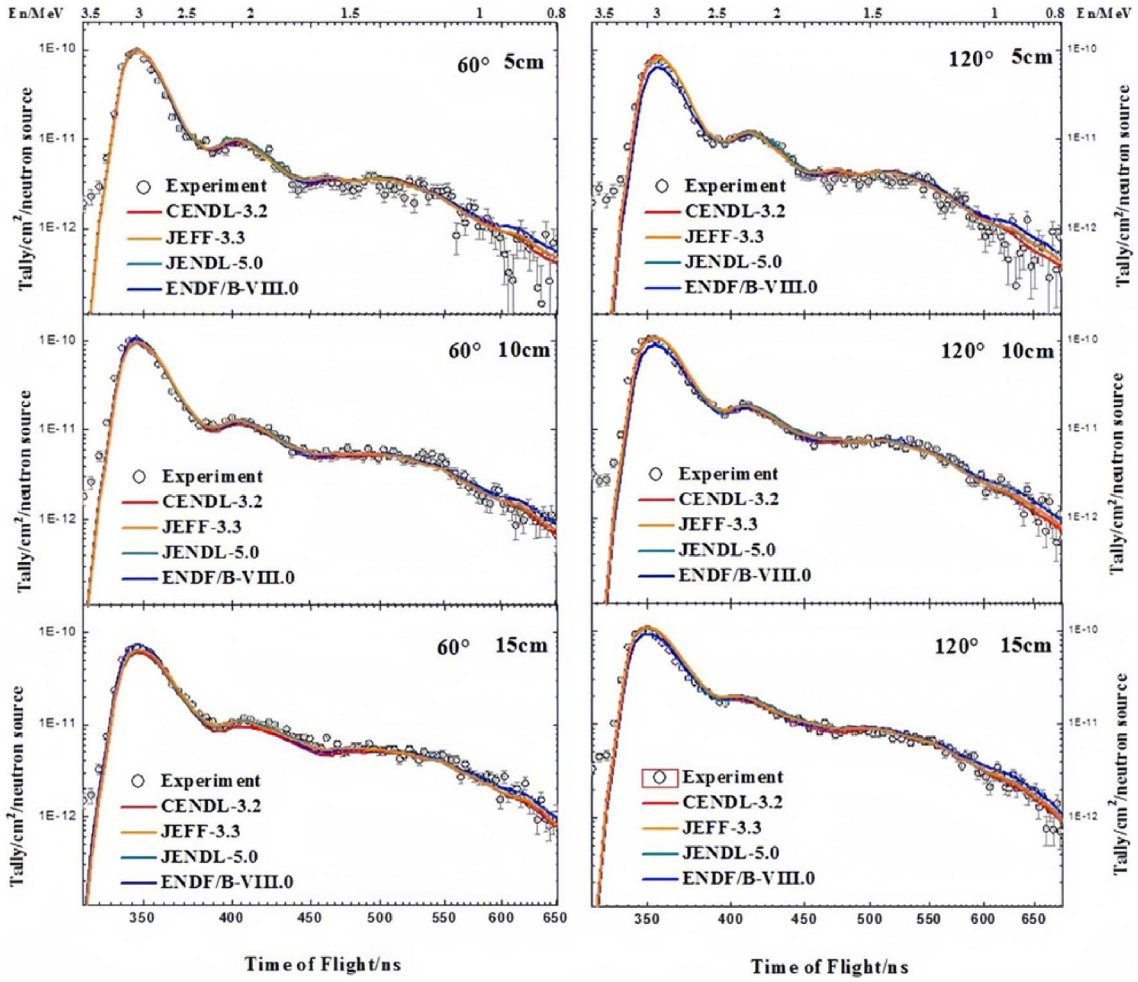

Fig. 10 The ToF spectra from the ^{nat}Pb sample after interaction with D-D neutrons

overestimated at 120°. This is possibly because the neutron spectra of (n,el) and (n,inl) retrieved from CENDL−3.2 and ENDF/B-VIII.0 were higher than those of the other two, as presented in Fig. 9. The results from JENDL−5 and JEFF−3.3 were underestimated at 60°, probably because JENDL−5 and JEFF−3.3 had lower values at 60° in the angular distribution of discrete-level inelastic scattering retrieved from JENDL−5 and JEFF−3.3. In summary, the angular distributions of (n,el) and (n,inl)D and the secondary neutron energy distribution of (n,inl)C for the ^{nat}Pb from CENDL−3.2 at an incident neutron energy of 14.5 MeV may need to be improved in future studies.

Table 5 C/E values of two energy regions and the total energy region

Angle	Thickness (cm)	Energy (MeV)	Time (ns)	CENDL−3.2	JEFF−3.3	JENDL−5	ENDF/B-VIII.0
60°	5	2.8-−3.5	320–352	1.054 ± 0.055	1.029 ± 0.054	1.013 ± 0.053	1.029 ± 0.054
		0.8-−2.8	352–652	1.136 ± 0.060	1.112 ± 0.059	1.153 ± 0.061	1.142 ± 0.060
		0.8-−3.5	320–652	1.091 ± 0.057	1.067 ± 0.055	1.077 ± 0.056	1.081 ± 0.056
	10	2.8-−3.5	320–352	0.860 ± 0.045	0.955 ± 0.050	0.866 ± 0.045	0.878 ± 0.046
		0.8-−2.8	352–652	0.932 ± 0.048	0.959 ± 0.050	0.975 ± 0.051	0.975 ± 0.051
		0.8-−3.5	320–652	0.918 ± 0.047	0.978 ± 0.050	0.945 ± 0.049	0.950 ± 0.049
	15	2.8-−3.5	320–352	0.860 ± 0.045	1.053 ± 0.055	0.899 ± 0.047	0.917 ± 0.048
		0.8-−2.8	352–652	0.833 ± 0.043	0.899 ± 0.046	0.897 ± 0.046	0.903 ± 0.047
		0.8-−3.5	320–652	0.864 ± 0.044	0.979 ± 0.050	0.921 ± 0.047	0.931 ± 0.048
120°	5	2.8-−3.5	330–368	1.086 ± 0.057	0.802 ± 0.042	1.048 ± 0.055	1.056 ± 0.055
		0.8-−2.8	368–680	1.077 ± 0.057	1.061 ± 0.056	1.112 ± 0.058	1.097 ± 0.058
		0.8-−3.5	330–680	1.082 ± 0.056	0.915 ± 0.047	1.076 ± 0.056	1.074 ± 0.055
	10	2.8-−3.5	330–368	1.000 ± 0.052	0.801 ± 0.041	0.980 ± 0.050	0.993 ± 0.051
		0.8-−2.8	368–680	0.988 ± 0.051	1.001 ± 0.052	1.044 ± 0.054	1.033 ± 0.053
		0.8-−3.5	330–680	0.995 ± 0.051	0.895 ± 0.046	1.010 ± 0.052	1.012 ± 0.052
	15	2.8-−3.5	330–368	1.080 ± 0.056	0.929 ± 0.048	1.065 ± 0.055	1.083 ± 0.056
		0.8-−2.8	368–680	1.007 ± 0.052	1.046 ± 0.054	1.073 ± 0.055	1.068 ± 0.055
		0.8-−3.5	330–680	1.044 ± 0.054	0.986 ± 0.051	1.069 ± 0.055	1.076 ± 0.055

Acknowledgements The authors express their gratitude to Hong-Tao Chen. and Kai Zhang. for operating the Cockcroft–Walton accelerator at the CIAE. This work was supported by the Research and development project of China National Nuclear Corporation.

Author contributions All authors contributed to the study conception and design. Material preparation, data collection and analysis were performed by Yang-Bo Nie, Yan-Yan Ding and Qi Zhao. The first draft of the manuscript was written by Kuo-Zhi Xu and all authors commented on previous versions of the manuscript. All authors read and approved the final manuscript.

Data availability The data that support the findings of this study are openly available in Science Data Bank at https://cstr.cn/31253.11.sciencedb.j00186.00342 and https://www.doi.org/10.57760/sciencedb.j00186.00342.

Declarations

Conflict of interest The authors declare that they have no Conflict of interest.

References

1. Z.Z. Ren, Y.W. Yang, Y.H. Chen et al., Measurement of the ^{232}Th(n, f) cross-section in the 1–200 MeV range at the CSNS Back-n. Nucl. Sci. Tech. **34**, 115 (2023). https://doi.org/10.1007/s41365-023-01271-7
2. X.R. Hu, G.T. Fan, W. Jiang et al., The measurements of ^{197}Au(n,γ) cross section up to 100 keV at the CSNS Back-n facility. Nucl. Sci. Tech. **32**, 101 (2021). https://doi.org/10.1007/s41365-021-00931-w
3. X.Y. Liu, Y.W. Yang, R. Liu et al., Measurement of the neutron total cross section of carbon at the back-n white neutron beam of CSNS. Nucl. Sci. Tech. **30**, 139 (2019). https://doi.org/10.1007/s41365-019-0660-9
4. J.Y. Tang, Q. An, J.B. Bai et al., Back-n white neutron source at CSNS and its applications. Nucl. Sci. Tech. **32**, 11 (2021). https://doi.org/10.1007/s41365-021-00846-6
5. Y. Oyama, H. Maekawa, Measurement and analysis of an angular neutron flux on a beryllium slab irradiated with deuterium-tritium neutrons. Nucl. Sci. Eng. **97**, 220–234 (1987). https://doi.org/10.13182/NSE87-A23504
6. I. Murata, T. Nishio, T.T. Kondo et al., benchmark experiments on $LiAlO_2$, Li_2 TiO_3 and Li_2 ZrO_3 assemblies using D-T neutron leakage neutron spectrum measurements. Fusion Eng. Des. **51–52**, 821–827 (2000). https://doi.org/10.1016/S0920-3796(00)00200-3
7. D.V. Markovskij, A.I. Blokhin, V.A. Chirkin et al., Integral benchmark experiments with 14 MeV neutrons for testing the nuclear data of vanadium. Fusion Eng. Des. **69**, 419–423 (2003). https://doi.org/10.1016/S0920-3796(03)00084-X
8. R. Liu, Y. Chen, H.P. Guo et al., Measurement of absolute reaction rates in Be, Pb and Fe spherical systems. Nucl. Sci. Tech. **9**, 2 (1998)
9. Q. Wang, B.J. Chen, Q. Zhang et al., Cross-sectional measurement of (n,2n) reactions for Nd isotopes induced by 14 MeV neutrons. Nucl. Sci. Tech. **30**, 8 (2019). https://doi.org/10.1007/s41365-018-0535-5
10. C.L. Lan, B.L. Xie, K. Zhang et al., of ^{232} Th (n , 2 n)^{231}Th reaction cross sections at neutron energies of 14.1 MeV and 14.8 MeV using the neutron activation method. Nucl. Sci. Tech. **26**, 6 (2015). https://doi.org/10.13538/j.1001-8042/nst.26.060501
11. L. Zhang, H.W. Yu, Y. Li et al., Improved formation density measurement using a controllable D-D neutron source and lithological correction for porosity prediction. Nucl. Sci. Tech. **33**, 3 (2022). https://doi.org/10.1007/s41365-022-00988-1
12. W.A. Metwally, S. El-Sayed, A. Ababneh et al., Flux measurements of DD neutron generator using neutron activation analysis. Nucl. Sci. Tech. **29**, 52 (2018). https://doi.org/10.1007/s41365-018-0385-1

13. J.M. Xue, S. Feng, Y.H. Chen et al., Measurement of the neutron-induced total cross sections of Pb from 0.3 eV to 20 MeV on the Back-n at CSNS. Nucl. Sci. Tech. **35**, 18 (2024). https://doi.org/10.1007/s41365-024-01370-z
14. Y.C. Wu, M. Wang, Q. Huang, Development status and prospects of Lead-based reactors. Nucl. Sci. Eng. **35**, 213–221 (2015). (in Chinese)
15. S.S. Kapoor, Accelerator-driven subcritical reactor system (ADS) for nuclear energy generation. Pramana **59**, 941–950 (2002). https://doi.org/10.1007/s12043-002-0143-z
16. P.A. Gokhale, S. Deokattey, V. Kumar, Accelerator driven systems (ADS) for energy production and waste transmutation: international trends in R.D. Prog. Nucl. Energy **48**, 91–102 (2006)
17. J.D. Court, R.C. Brockhoff, J.S. Hendricks, Lawrence Livermore pulsed-sphere benchmark analysis of MCNP (trademark) ENDF/B-VI, Los Alamos National Laboratory Report LA-12885, December (1994)
18. A.A. Androsenko, P.A. Androsenko, B.V. Derkin et al., Measurements and comparison with calculations of neutron leakage spectra from U, Pb, Be spheres with a central 14 MeV neutron source. Kernenergie **10**, 422 (1988)
19. S.P. Simakov, A.A. Androsenko, P.A. Androsenko et al., Neutron leakage spectra of Be, Al, Fe, Ni, Pb, LiPb, Bi, U, and Th spheres with T(d, n) and ^{252}Cf neutron sources. Fusion Technol. **1992**, 1489–1493 (1992). https://doi.org/10.1016/B978-0-444-89995-8.50292-7
20. H. Maekawa, Y. Oyama, Experiment on angular neutron flux spectra from lead slabs bombarded by D-T neutrons. Fusion Eng. Des. **18**, 287–291 (1991). https://doi.org/10.1016/0920-3796(91)90140-L
21. J. Briesmeister, (Ed.), MCNP-general Monte Carlo N-particle transport code system, Version 4C, Report LA-13709-M, 2000
22. Z.G. Ge, R.R. Xu, H.C. Wu et al., CENDL-3.2: The new version of Chinese general purpose evaluated nuclear data library. EPJ Web Conf. **239**, 09001 (2020) .doi: https://doi.org/10.1051/epjconf/202023909001
23. O. Cabellos, F.A. Velarde, M. Angelone et al., Benchmarking and validation activities within JEFF project. Eur. Phys. J. Conf. (2017). https://doi.org/10.1051/epjconf/201714606004
24. O. Iwamoto, N. Iwamoto, S. Kunieda et al., Japanese evaluated nuclear data library version 5: JENDL-5. J. Nucl. Sci. Technol. **60**, 1–60 (2023). https://doi.org/10.1080/00223131.2022.2141903
25. D.A. Brown, M.B. Chadwick, R. Capote et al., ENDF/B-VIII.0: the 8th major release of the nuclear reaction data library with CIELO-project cross sections, new standards, and thermal scattering data. Nucl. Data Sheets **148**, 1–142 (2018). https://doi.org/10.1016/j.nds.2018.02.001
26. S. Zhang, Y.B. Nie, J. Ren et al., Benchmarking of JEFF-3.2, FENDL-3.0, and TENDL-2014 evaluated the data for tungsten with 14.8 MeV neutrons. Nucl. Sci. Tech. **28**, 27 (2017). https://doi.org/10.1007/s41365-017-0192-0
27. Y.B. Nie, J. Ren, X.C. Ruan et al., Benchmarking of evaluated nuclear data for iron using ToF experiments with slab samples. Fusion Eng. Des. **145**, 40–45 (2019). https://doi.org/10.1016/j.fusengdes.2019.05.021
28. Y.Y. Ding, Y.B. Nie, J. Ren et al., Benchmark experiment for bismuth using slab samples with D-T neutron source. Fusion Eng. Des. **167**, 112312 (2021). https://doi.org/10.1016/j.fusengdes.2021.112312
29. Y.Y. Ding, Y.B. Nie, J. Ren et al., Benchmark experiment on slab iron with D-T neutrons to validate evaluated nuclear data. Ann. Nucl. Energy **132**, 236–242 (2019). https://doi.org/10.1016/j.anucene.2019.04.041
30. Y.Y. Ding, Y.B. Nie, Y. Zhang et al., A benchmark experiment on slab ^{238}U with D-T neutrons to validate the evaluated nuclear data. Nucl. Sci. Tech. **35**, 29 (2024). https://doi.org/10.1007/s41365-024-01386-5
31. Q. Zhao, Y.B. Nie, Y.Y. Ding et al., Measurement and simulation of leakage neutron spectra from Fe spheres bombarded with 14 MeV neutrons. Nucl. Sci. Tech. **34**, 182 (2023). https://doi.org/10.1007/s41365-023-01329-6
32. Q.P. Zhong, X.J. Chen, H.L. Lu et al., Background analysis of an associated particle method for measuring the neutron fluence rate from T(d, n)^{4}He neutron source. Atom. Energ. Sci. Technol. **39**, 131–133 (2000). https://doi.org/10.7538/yzk.2005.39.02.0130. (**in Chinese**)
33. T.H. Zhu, R. Liu, L. Jiang et al., The associated proton-monitoring technique of the D-D source neutron yields at a large angle. Nucl. Electron. Detect. Technol. **27**, 141–145 (2007). (**in Chinese**)
34. L. Ruby, R.B. Crawford, Anisotropy factors for determining the total neutron yield from D(d, n)^{3}He, and T(d, n)^{4}He reactions. Nucl. Instrum. Methods **24**, 413–417 (1963). https://doi.org/10.1016/0029-554X(63)90358-6
35. J.Z. Li, P.G. Fan, H.L. Lu et al., Cheak two methods for measuring D(d, n) neutron flux. Atom. Energ. Sci. Technol. **16**, 14–17 (1982). https://doi.org/10.7538/yzk.1982.16.01.0014. (**in Chinese**)
36. X.G. Cai, Y.B. Nie, J. Bao et al., Design of a precollimator system for neutronics benchmark experiments. Nucl. Tech. **36**, 010201 (2013). https://doi.org/10.11889/j.0253-3219.2013.hjs.36.010201. (**in Chinese**)
37. D. Schlegel, *TARGET User's Manual* (Physikalisch-Technische Bundesanstalt, Braunschweig, 2005)
38. R. Marcel, *The "Multi-Channel'' Unfolding Programs in the UMG Package: MXD-MC32 and IQU-MC32, and GRV-MC32* (Physikalisch-Technische Bundesanstalt, Braunschweig, 2003)
39. Y.B. Nie, J. Ren, X.C. Ruan et al., Benchmark experiments with slab samples using the time-of-flight technique at the CIAE. Ann. Nucl. Energy **136**, 107040 (2020). https://doi.org/10.1016/j.anucene.2019.107040
40. J. Ren, Y.B. Nie, X.C. Ruan et al., Calibration of the neutron detection efficiency for a liquid scintillator with ^{252}Cf fission gamma rays, and time-of-flight methods. Atom. Energ. Sci. Technol. **52**, 215–220 (2018). https://doi.org/10.7538/yzk.2017.youxian.0258. (**in Chinese**)
41. G. Dietze, H. Klein, NRESP4 and NEFF4 Monte Carlo code for the calculation of neutron response functions and detection efficiencies for NE213 scintillation detectors. Physikalisch-Technische Bundesanstalt PTB-ND-22 (1982)
42. Y.Y. Ding, Y.B. Nie, J. Ren et al., Measurement and simulation of neutron leakage spectra with polyethylene samples of different sizes. Atom. Energ. Sci. Technol. **51**, 223–229 (2017). https://doi.org/10.7538/yzk.2017.51.02.0223. (**in Chinese**)
43. B. Zhang, X.B. Ma, K. Hu et al., Performance of CENDL-3.2 and other major neutron data libraries for criticality calculations. Nucl. Sci. Tech. **33**, 8 (2022). https://doi.org/10.1007/s41365-022-00994-3
44. R.E. Macfarane, D.W. Muri, R.M. Boicourt et al., NJOY nuclear data processing system. Version 6, LA-UR-17-20093, Los Alamos National Laboratory, December 2016
45. K. Zhang, Y.B. Nie, J. Bao et al., Verification of integral experimental system using standard sample method. Nucl. Tech. **37**, 080501 (2014). https://doi.org/10.11889/j.0253-3219.2014.hjs.37.080501. (**in Chinese**)
46. Y.L. Jin, X. Tao, J.M. Wang et al., NDplot: plotting tool for nuclear data. EPJ Web Conf. **239**, 10004 (2020). https://doi.org/10.1051/epjconf/202023910004